

Øgon, A REVOLUTIONARY NEW LENS FREE OPTICAL SCANNER (LFOS) FOR ADDITIVE MANUFACTURING (AM)

C. Bibas

Tecnica, Inc. 175 East Shore Rd. Great Neck, NY 11023

Abstract

The core engine of an SLS/SLM AM printer is the Optical Scanner. Typically, either a galvanometer (GS) or a Polygonal Mirror (PM) scanner has been used, but both have been pushed to their mechanical limits. Both scanners suffer from inconsistency in energy deposition because of changes in Optical Path Length (OPL), Surface Beam Speed (SBS), and angle of incidence (θ).

The Øgon™ Lens Free Optical Scanner (patented by Tecnica, Inc., Great Neck, New York), on the other hand, provides a simple scanning method, linear transfer functions, fixed OPL, and an incident beam normal to the work surface. This paper describes the optics of the Øgon™ and compares it head to head with the GS. The study shows the Øgon™ delivers a linear transfer function, where the optical path length, surface beam speed, and θ , the angle of incidence (and therefore the beam size and shape) are constant.

A substantially improved version of this paper appears in a special issue of the TMS publication *JOM*, March 2022.

Introduction

PM scanners and GS have been used for more than four decades in 2D and 3D printing. Both technologies have been improved with better optomechanical controlling systems, better optics, and better manufacturing capabilities. These incremental improvements to the existing technologies have significantly improved the quality of the model parts. However, as much as the technology can offer, there are fundamental limits that prevent further improvements. Specifically, the optical path length, surface beam speed, and incident beam angle to the surface (which affect the beam size and shape) unavoidably vary as the beam scans the work surface. This means that the energy deposition and therefore surface temperature per pixel will vary and be difficult to control. Numerous studies, as an example [1], [2], [3], [4] developed predicting models attempting to analyze and control the temperature distribution in Metal additive printing.

In contrast, the energy deposition is constant in the Øgon™ system because the beam is always perpendicular to the work surface. This property by itself makes the Øgon™ scalable.

In this paper, we'll be exploring the limits of the currently employed optical scanners and their readiness for AM production and specifically for metal printing, in which temperature prediction is a crucial parameter.

Mathematical models are used to produce a system capability chart for each scanning system where pros and cons for each scanner are spelled out and compared.

Methods

The GS system is analyzed with the post-objective scanning method, in which the scanner is positioned post the objective lens. The rays converge to be focused at the work surface even though the beam source is collimated. Choosing this method exposes optical system weakness in comparison to the pre-objective method.

Although in this paper, we analyze the GS and compare it to the Øgon™, the PM has similar results as the GS. The optomechanical systems of the GS and Øgon™ scanning systems are mathematically analyzed and compared with regards to:

Modulation:

The modulator is the control unit controlling the GS. The modulator provides the electrical signals to the GSx and GSy for positioning the laser beam on the desired spot location.

OPL:

Optical Path Length is the optical beam length from the beam source or a reference point to the work area. Any change in the OPL will cause degradation in optical performance such as loss of focus (beam enlargement).

Positioning:

Positioning is analyzed by looking into the full range of the scan area, as well as coordinate symmetry and linearity. Asymmetry, scaling, and nonlinearity affect the modulator by adding complexity. As an example, when controlling GSx

$$x(a \cdot \theta_0) \neq a \cdot x(\theta_0)$$

This imposes a nonlinear scaling control of the modulator.

Resolution:

The resolution is affected by various factors, including positioning, beam speed acceleration/deceleration, and the use of open vs closed-loop modulators.

Scalability:

The ability to print/scan large areas is an indication of good scalability.

Beam Speed:

Beam speed is analyzed because changes in beam speed affect the total amount of energy delivered to each pixel. A higher speed means less time on each pixel → less energy.

Θ (Capitalized theta):

Θ is the angle of incidence, which is defined as the angle between the incident beam and the normal to the surface.

Beam energy density:

The energy density of a beam is defined by: $Ed = E/A$, where A is the beam size at the work surface. The energy absorbed by the surface attributed to Θ is quantified by [5]:

$$Ed \approx E_0 \cdot \cos^4(\Theta)$$

Where E_0 is the maximum energy.

Beam size and shape:

Beam size and shape is a dependent property that is affected directly by OPL and Θ reflecting the change in focus as well as changes in incidence angle with the work surface.

Repeatability:

The difference in resulting position of the GS when given the same command input multiple times in a row, measured in microradians.

Offset Error:

In electromechanical devices such as a GS, the modulator suffers from offset errors; there is a shift or drift of the origin, in which a command calling for a zero origin will produce a non-zero location. This error will be magnified by changes in temperature.

Linearity Error:

A linearity error of a system is the maximum deviation of the transfer characteristic from a prescribed straight line.

Temperature prediction:

One of the most important properties in AM for metal is the prediction of the temperature induced by the laser beam [1],[2]. The prediction is used to mitigate the non-uniform temperature distribution across the top layer as well as the gradient temperature across the other layers below. A non-uniform temperature will cause thermal stress to appear on the model [1] causing tensile residual stress on the surface and acceleration of crack propagation.

Mathematical models are used to produce a system capability chart for each scanning system where pros and cons for each scanner are spelled out and compared.

Galvanometer: Advantages and Limitations

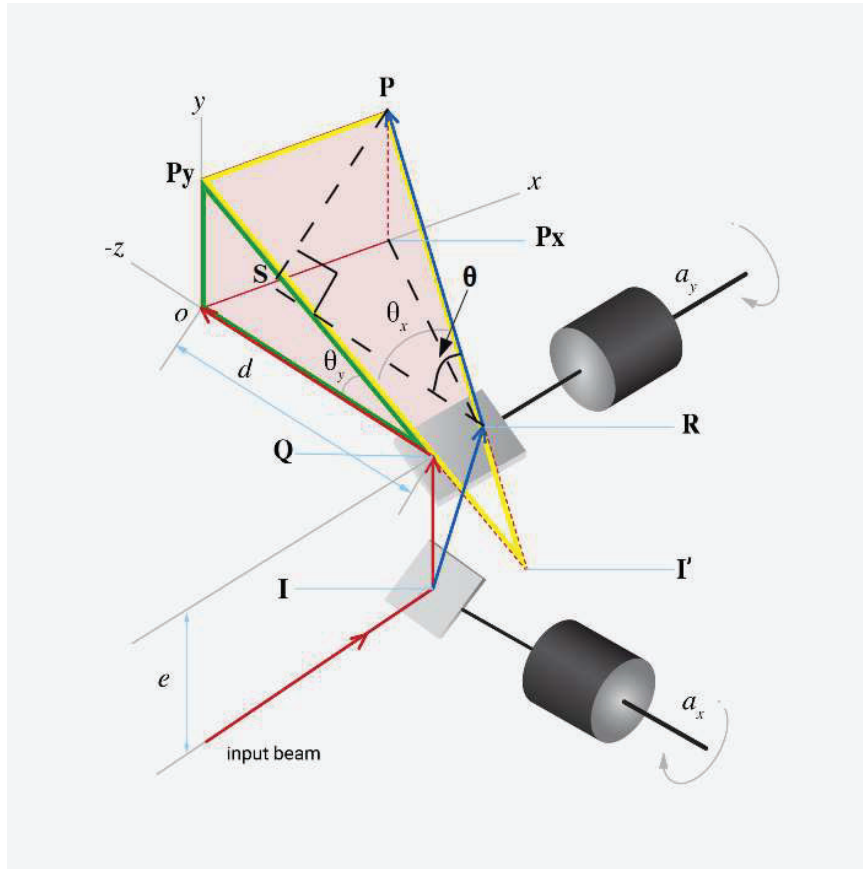


Figure 1. GS Optical Scanner composed of two Galvanometers in 2D scanning setting

Transfer functions are functions representing the beam properties as an output where the input is the command parameter(s). For the GS system, the transfer functions are a function of θ_x, θ_y (input) where $\theta_x = 2 \cdot \omega_x \cdot t$, $\theta_y = 2 \cdot \omega_y \cdot t$ respectively where $\omega \cdot t$ is the angular rotation of the respective motor.

Position:

Beam location [6]:

$$y(\theta_y) = d \cdot \tan(\theta_y) \quad (1)$$

$$x(y, \theta_x) = (\sqrt{d^2 + y^2} + e) \cdot \tan(\theta_x) \quad (2)$$

$$x(\theta_x, \theta_y) = (d \cdot \sqrt{1 + \tan^2(\theta_y)} + e) \cdot \tan(\theta_x) \quad (1)(2)$$

Symmetry:

It is evident from eq (1) that there is symmetry about the origin for GSy where $y(-\theta_y) = -y(\theta_y)$. Similarly, from eq (2) GSx is symmetrical when θ_y is held constant where

$x(-\theta_x, \theta_0) = -x(\theta_x, \theta_0)$ for $\theta_y = \theta_0$ Please also note that x is a function of two inputs θ_x and θ_y .

Beam speed:

$$V_x(\theta_x) = dx/d\theta_x = d [(d \cdot \sqrt{1 + \tan^2(\theta_y)} + e) \cdot \tan(\theta_x)]/d\theta_x \quad (3)$$

$$V_x(\theta_x) = (d \cdot \sqrt{1 + \tan^2(\theta_y)} + e) \cdot 1/\cos^2(\theta_x) \quad (3)$$

$$V_y(\theta_y) = dy/d\theta_y = d [d \cdot \tan(\theta_y)] / d\theta_y = d \cdot 1/\cos^2(\theta_y) \quad (4)$$

Where the surface speed is the vector sum:

$$V = \sqrt{V_x^2 + V_y^2} \quad (5)$$

$$V = \sqrt{((\sqrt{d^2 + y^2} + e)^2/\cos^4(\theta_x) + d^2/\cos^4(\theta_y))} \quad (5)$$

$$V = \sqrt{(d \cdot \sqrt{1 + \tan^2(\theta_y)} + e)^2/\cos^4(\theta_x) + d^2/\cos^4(\theta_y)} \quad (5)$$

eq (1) (2) shows that:

$$y(\theta_0) \neq x(\theta_0) \quad \text{for } \theta_y = \theta_x = \theta_0$$

Additionally, it is evident from eq (3) (4) that:

$$V_x(\theta_0) \neq V_y(\theta_0) \quad \text{for } \theta_y = \theta_x = \theta_0$$

Not only are the transfer functions for V_x and V_y different, but to add further complications, the surface speed is the vector sum of the two. The asymmetry in speed is further augmented as the surface senses the vector sum of V_x and V_y . This property (V) is difficult to control as it is dependent on the print path of the rendering vector.

Optical Path Length (OPL):

OPL is the Optical Path Length where $OPL = PI'$ measured from the beam source I or I' to the beam incident point on the x - y surface P where:

$$PI'^2 = x^2 + (\sqrt{y^2 + d^2} + e)^2 \quad (6)$$

Alternatively, it can be expressed as a function of (θ_x, θ_y)

$$OPL = (d \cdot \sqrt{1 + \tan^2(\theta_y)} + e) \cdot \sqrt{1 + \tan^2(\theta_x)} \quad (6)$$

OPL is a product of two non-linear functions that change quickly as the beam moves away from the origin (print center). OPL is also one of the parameters affecting the beam's focus and therefore its intensity.

Θ (Capitalized Theta):

Θ , the angle of incidence, is the angle between the incident beam and the normal to the surface. It is calculated from triangle $P P_x R$:

$$\Theta = \arccos \left[d / \left(\sqrt{x^2 + (\sqrt{d^2 + y^2} + e)^2} - e/\cos(\theta_x) \right) \right] \quad (7)$$

Alternatively, it can be expressed as a *function of* (θ_x, θ_y) :

$$\Theta = \arccos \left\{ 1 / \left[\left(\sqrt{1 + \tan^2(\theta_y)} + e/d \right) \cdot \sqrt{\tan^2(\theta_x) + 1 - e/(d \cdot \cos(\theta_x))} \right] \right\} \quad (7)$$

Equation (7) shows that Θ changes across the scan area. Θ is also one of the parameters affecting the beam intensity.

Beam size and shape:

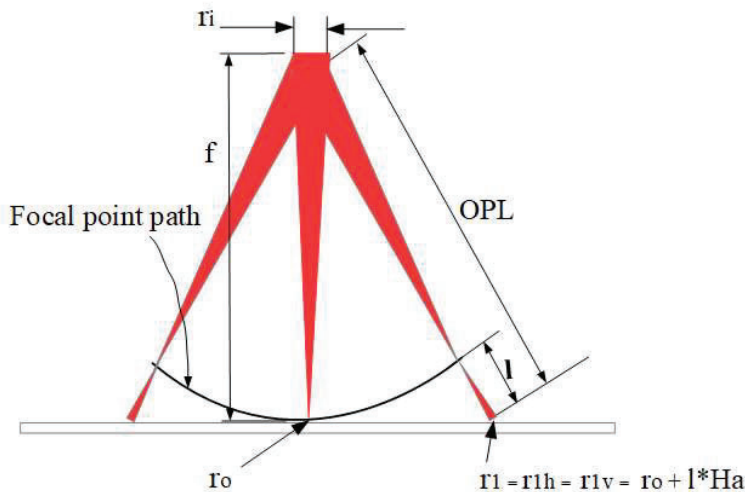


Figure 2. OPL induced beam enlargement

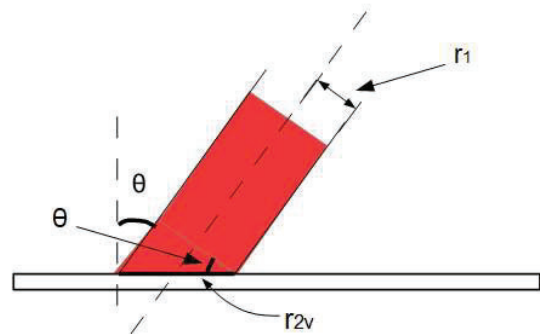


Figure 3. Θ induced beam enlargement

Consider a circular beam with radius r_0 and at focus at the origin: as the beam moves across the work surface, beam size and shape will change as Θ and OPL change.

As the beam traverses the surface and Θ deviates from zero, the beam's image on the surface stretches from a circle to an ellipse. Denote the vertical ellipse axis r_v and the horizontal axis r_h to be the ellipse axes where v and h are the local coordinates of the image lying on the work

surface. Intentionally, they are not marked minor or major axes as minor, and major will be switching places depending on the location on the work surface. Beam augmentation is analyzed in two stages wherein state 1 is the effect due to OPL and state 2 is the effect due to Θ .

The two stages are quantified by:

Beam radius change as a result of OPL (stage 1):

Assuming the system focuses at the origin where $\theta_x = 0$ and $\theta_y = 0$ is at $f = d + e$ distance from the work surface where Ha (half-angle for a converging beam) can be extracted from f and GS mirror size. Then calculating beam enlargement by *OPL* :

where r_{1v}, r_{1h} are the ellipse beam axes projected on the work surface:

$$r_1 = r_{1v} = r_{1h} = r_0 + l \cdot Ha \quad (8)$$

where

$$l = OPL - (d + e) = (d \cdot \sqrt{1 + \tan^2(\theta_y)} + e) \cdot \sqrt{1 + \tan^2(\theta_x)} - (d + e) \quad (9)$$

$$r_1 = r_0 + \left((d \cdot \sqrt{1 + \tan^2(\theta_y)} + e) \cdot \sqrt{1 + \tan^2(\theta_x)} - (d + e) \right) \cdot Ha \quad (8)(9) \rightarrow (10)$$

Beam radius change as a result of Θ (stage 2) :

Only the local vertical axis is changing where:

$$r_{2v} = r \cdot 1/\cos(\Theta) \quad (11)$$

$$r_{2h} = r_1 \quad (12)$$

$$r_{2v} = \left((\sqrt{1 + \tan^2(\theta_y)} + e/d) \cdot \sqrt{\tan^2(\theta_x) + 1} - e/(d \cos(\theta_x)) \right) \cdot \left(r_0 + \left((d \cdot \sqrt{1 + \tan^2(\theta_y)} + e) \cdot \sqrt{1 + \tan^2(\theta_x)} - (d + e) \right) \cdot Ha \right) \quad (13)$$

Beam area is calculated by:

$$A = \pi \cdot r_{h2} \cdot r_{v2} = \pi \cdot r_1^2 \cdot 1/\cos(\Theta) \quad (14)$$

substituting $1/\cos(\Theta)$ with eq (7):

$$A = \pi \cdot \left(r_0 + \left((d \cdot \sqrt{1 + \tan^2(\theta_y)} + e) \cdot \sqrt{1 + \tan^2(\theta_x)} - (d + e) \right) \cdot Ha \right)^2 \cdot \left((\sqrt{1 + \tan^2(\theta_y)} + e/d) \cdot \sqrt{\tan^2(\theta_x) + 1} - e/(d \cdot \cos(\theta_x)) \right) \quad (14)$$

It is apparent from eq (14) that the energy density E/A changes as the beam moves across the work surface. Moreover, eq (14) is not symmetrical when relating to θ_x and θ_y in addition to not being symmetrical for x,y coordinates as:

$$y(\theta_x) \neq x(\theta_y)$$

$$A(x,y) \neq A(y,x)$$

Most importantly, $\tan(\theta_x)$, $\tan(\theta_y)$ components change nonlinearly as the angles grow. It causes sharper growth in A as θ_x , θ_y grows. The asymmetry in A augmentation needs to be considered for each pixel. Therefore, the modulator needs to be configured to take into account these non-linearities and asymmetry. This also means that part positioning on the x-y bed matters.

Furthermore, the speed also is not symmetrical where $V(\theta_x) \neq V(\theta_y)$. This further highlights the asymmetry in energy deposition where the beam speed is one of the dictating parameters for the energy density absorbed by the surface.

Linearity:

It is apparent from eq (1) and (2) that the transfer function for either x or y is nonlinear. The use is limited to small angles where $\tan(\theta_x)$, $\tan(\theta_y)$ is close to linear. It is evident from eq (7) that e , the distance between GSx and GSy must be kept as small as possible in relation to d , the distance between GSy and the work surface. The smaller e/d the smaller the Θ .

Modulation:

Modulation in a GS system is performed using a closed loop. The challenges are in addressing nonlinearity transfer functions (position, speed, energy deposition for printing) and the mechanical inertia of the oscillatory element in the GS. As the transfer functions are not linear, adjustments need to be performed. The nonlinear positioning can be addressed by geometric correction techniques Xianyu [7]. Similarly, Zhang [8] is further measuring data spots and performing an online calibration on the GS. Furthermore, the nonlinearity in speed can be addressed with an f-theta lens where $\tan(\text{angle})$ is converted to the *angle* itself. However, f-theta manufacturing constraints limit its maximum size and therefore, are not scalable.

Duma [9] further explored the GS mechanical inertia of the oscillatory element limitation where he qualifies the modulation speed limit to be around 1.5Khz and selected the preferred/optimized modulation waveform to be a saw wave with fast and slow-moving GS where the raster method is used.

Offset/Drift Errors:

Offset/drift errors happen when the GS deviates from the origin and as a result moves all respective coordinates. Offset/drift errors are temperature sensitive and need to be watched closely. Offset/drift errors can be addressed by an online correction on the fly in a similar method to Zhang [8].

Offset Errors are measured in microradians. A typical value from a quality GS manufacturer is less than 10 microradians. Some manufacturers, unfortunately, amplify the offset/drift error when they make design choices to reduce the Θ -related errors. As an example, a company may

enlarge **d** - the distance from the GSy to the work surface - from 500 cm to 2000 cm. Enlargement of **d** will reduce the max Θ required for the same size work surface, therefore reducing Θ related errors, but amplifying offset/drift errors.

Consider a 0.1 mm beam diameter using a hach (grid) of 0.1mm. The position is now dictated by a longer arm **d**. A typical 5 microradian offset/drift error will result in a 10 microradian error in Θ .

Intended location at x_0

$$\text{New location: } x_0 \pm \text{Err} = x_0 \pm d \cdot 10\text{urad} = x_0 \pm 20\text{um}$$

This is already a change of 20% of the grid size. Temperature changes will amplify this error by a factor proportional to the temperature change. As an example, Cambridge Technology for their GS model 83xxK spec shows a Zero Drift parameter to be at 5 urad/°C. A change of 7 °C will inflict a position change (for a d=2000 mm) of:

$$x_0 \pm \text{Err} = x_0 \pm 5 \cdot 2 \cdot 10^6 \cdot 7\text{urad} = x_0 \pm 70\text{um}$$

Please also note: this error is only for one GS. Adding the second GS vector will inflict a total Grid shift of $\pm \sqrt{2} \cdot 70\text{um} \rightarrow \pm 99\text{um}$.

Repeatability:

Repeatability error is measured in microradians units. It is doubled when reflecting from the GS mirror. Additionally, the error is further augmented when GSx & GSy errors are combined. A typical repeatability error value for a single GS is 5-10 microradians.

Temperature prediction:

Energy deposition across the work area depends mostly on Θ and the print path. Consider when the beam is moving away from the origin from voxel n to voxel (n+1): the elongation of the beam shape on the surface means that, while the beam is activated for voxel n, voxel (n+1) will be preheated. In contrast, when the beam is moving towards the origin, the next voxel is not preheated. This asymmetry further contributes to the non-uniform temperature distribution.

Conclusions for GS:

Although the **GS** provides **2D** scanning for the x and y dimensions. the asymmetry and nonlinearity in positioning and speed make it more challenging to modulate when high-resolution, high-quality print/scanning is needed. This is especially true for **AM**, where analog intensity level is important, in contrast to sensing.

Table 1 shows the impact of the coordinate asymmetry and nonlinearity transfer functions for d=25, e=5 where the **GS** is tested for different θ_x, θ_y . As any of the θ_x, θ_y grows, Θ grows.

The results also show that it is desirable to underutilize the **GS** in regards to Θ . Although some GS are capable of a Field Of View of $\pm 25^\circ$ or more, this range is not usable for AM as the absorbed energy drops quickly as Θ increases, as Table 1 illustrates:

	Intensity(%)	OPL	$\Theta(^\circ)$	x	y	$\theta_x(^\circ)$	$\theta_y(^\circ)$
1	98.487	30.115	5.00	2.625	0.000	5.000	0.000
2	96.996	30.210	7.07	2.633	2.187	5.000	5.000
3	92.637	30.502	11.17	2.658	4.408	5.000	10.000
4	87.051	30.882	15.00	0.000	6.699	0.000	15.000
5	87.051	31.058	15.00	8.038	0.000	15.000	0.000
6	67.469	33.101	25.00	13.989	0.000	25.000	0.000
7	67.469	32.584	25.00	0.000	11.658	0.000	25.000
8	45.520	35.953	34.78	15.194	11.658	25.000	25.000

Table 1. Intensity as a function of Θ

Although modulation of the y coordinate is dependent only on θ_y , modulation for the x coordinate depends on both θ_x and θ_y . Therefore, the x modulator needs additional input. Rows 1-3 and (6,8) illustrate clearly how x needs to be recalculated any time y is changing. This puts a burden on the modulator when rendering a vector because the print path must be calculated to produce the outputs for each GS. Additionally, the beam cross-section changes with Θ , inflicting additional degradation of absorbed energy at the surface.

Øgon: Advantages and Limitations

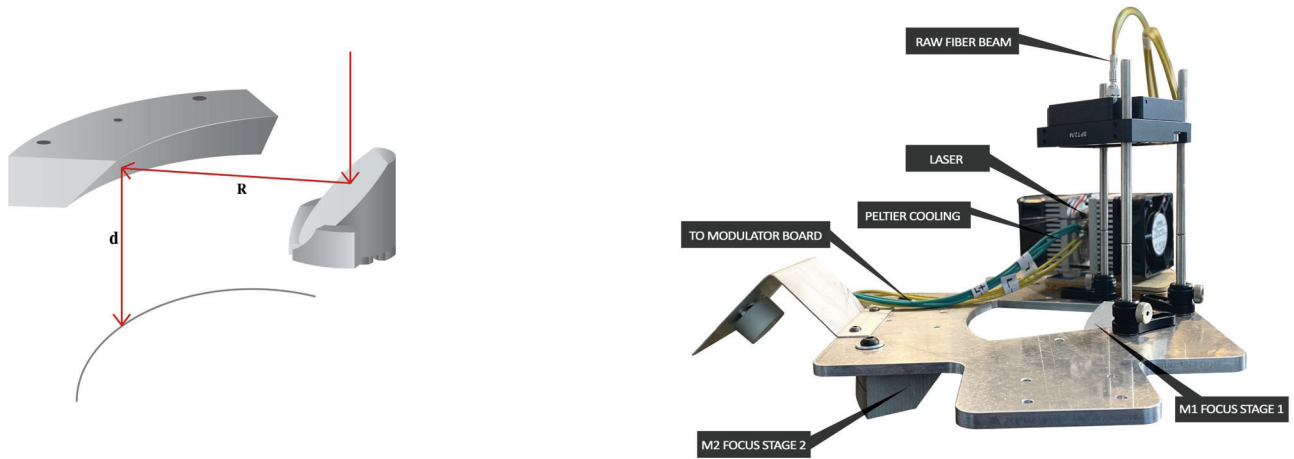


Figure 4. Øgon

The ØgonTM consists of two reflectors M1 and M2 where M1 is a rotating reflector and M2 an annular stationary reflector. The beam source strikes M1 along the optical axis, which is also the actuator rotational axis. The beam then travels towards M2, which diverts the beam to the work surface.

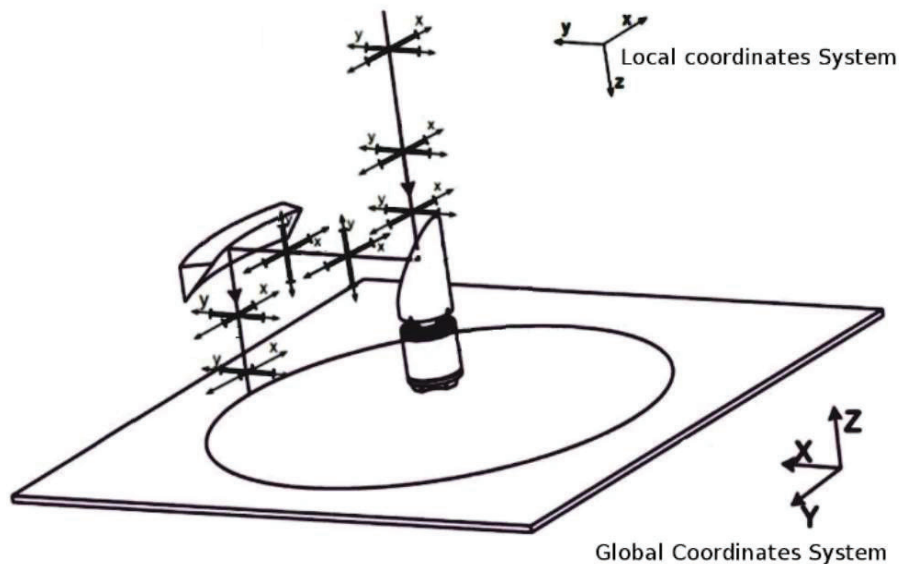


Figure 5. Øgon optical functionality Bibas [10], [11]

A simplified ØgonTM would be composed of a flat M1 reflector and an annular cone M2. However, because a conical M2 would modify the beam in one direction (x) only, while the

second direction (y) would remain unchanged, a collimated beam would be focused in only one direction as illustrated in Figure 6. The challenge for focusing the second dimension is solved [10] by modifying M1 from a flat to a concave mirror and M2 to a non conical surface where the surface formulas for both are calculated to produce a focus in the second direction as well.

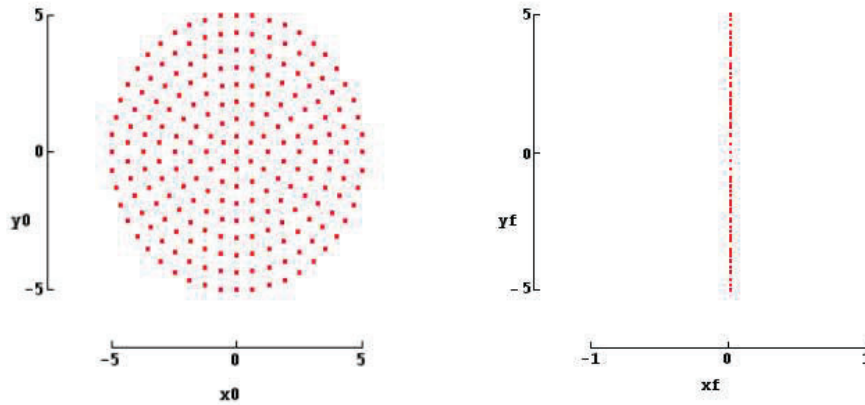


Figure 6. Cross-section of the beam source (left) and final beam cross-section at the work surface resulting from a flat M1 reflector and a conical shape M2.

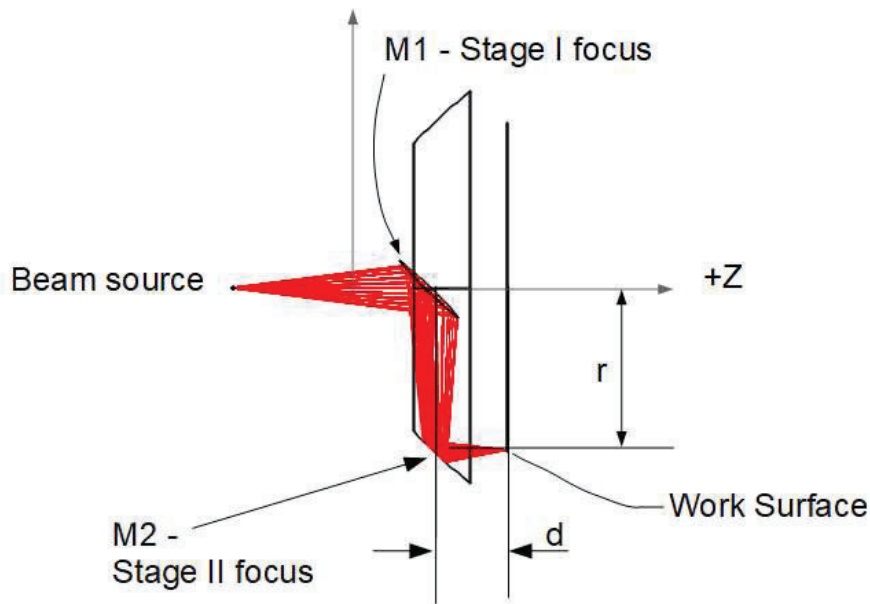


Figure 7. Øgon performs four functions: beam rotation, steering, rotation around its local axis, and focusing

Øgon™ functions performed on the beam source:

1. Beam steering: first, it is steered by M1 from the beam source optical axis, then by M2 back parallel to the beam source optical axis

2. Beam revolution around the beam source: the output beam revolves around the beam source optical axis
3. Beam rotation around its local optical axis
4. Beam focusing: the beam is fully focused in both directions at the worksurface

The Øgon™ focuses a diverging beam without the use of lenses. As an example, a beam source from multimode fiber with 105-micrometer cladding diameter and NA0.15 focuses back to the beam source size in the Øgon™ first prototype where $r=125\text{mm}$ and $d=60\text{mm}$.

Because the beam rotates around its own axis, it radiates more consistent energy.

Position:

Because the Øgon™ is a 1D scanner, it requires a conveyor for the second axis (the slow axis). In that way, it is similar to the PM in scanning operations. The raster scanning method is used where arcs are used for the first axis. A 2D scan is performed with a linear conveyor. Following each arc scan, the slow-moving conveyor moves an arc thickness. This method resembles PM 2D printing. However, the result is much superior to the PM as the PM must print on a cylindrical conveyor to keep the focus, while the Øgon™ is at focus printing on a flat surface. Additionally, the slow-moving conveyor wear and tear is very small compared, for example, to a CNC actuator as there is very little travel time during the Øgon™ print.

The hybrid system can be described by:

Øgon™ printhead:

The rotational speed at the work surface is controlled by the motor rotational speed (rotations per second f). As the beam is perpendicular to the work surface the beam path at the work surface follows the M2 curvature radius; therefore, beam location is simplified using polar coordinates:

Beam location θ where r is constant, Arc length $s(\theta) = \theta \cdot R$ or

$$s(t) = \omega \cdot t \cdot R = 2 \cdot \pi \cdot R \cdot f \cdot t$$

slow-moving conveyor:

The Øgon™ is carried by the conveyor, where beam position is expressed by:

$$\begin{aligned} y(t) &= Yc(t) + R \cdot \cos(2 \cdot \pi \cdot f \cdot t) && ; Yc \text{ is the conveyer location} \\ x(t) &= R \cdot \sin(2 \cdot \pi \cdot f \cdot t) \end{aligned}$$

Alternatively, the beam location in cartesian coordinate can be expressed with i and j :

$$\begin{aligned} y(i,j) &= i \cdot \Delta y + R \cdot \cos(2 \cdot \pi \cdot j/P) \\ x(j) &= R \cdot \sin(2 \cdot \pi \cdot j/P) \end{aligned}$$

Where Δy is the interval to move from the current position. Δy also represents the distance between the arcs, i is the arc number and j is the pixel location in the arc where $j=0$ when $x=0$. P is the number of pixels in a full circle.

Beam speed:

When the beam is activated the conveyor is not moving. Therefore, the surface speed is calculated by:

$$v(t) = ds/dt = 2 \cdot \pi \cdot R \cdot f$$

Where s is the arc travel length.

Scanning method:

The scanning is done by using arcs where the \Ogon^{TM} is carried by a linear actuator (y) to provide the second axis. This way, the scanning is performed in a raster where y is the slow-moving axis.

maximum scanning speed:

When M1 is carried by a brushless motor, where $f = 2000 \text{ Hz}$ (2000 rotations per seconds) when $R=125 \text{ mm}$ is selected, the surface print speed is:

$$2 \cdot \pi \cdot R \cdot f = 1570 \text{ meter/sec}$$

As a comparison, a GS print speed max speed is below 10 meters/Sec.

Repeatability:

A typical repeating error for the actuator used for the *Casa I printer* is 5 micrometers for every 100mm. The weak point in the polar system is the motor because tilt from the vertical axis will affect the positioning. The tilt is addressed by keeping the center of mass on the rotational axis.

OPL:

There is no change in OPL, hence it is: $2 \cdot (d + R)$. Where d is the distance from M2 to the work surface and R is the distance between M1 and M2.

Beam Size and Shape:

As the beam is at focus at any M1 angular position, the size and shape is constant, hence beam radius is: r_0 .

Θ (Capitalized Theta):

The beam is always normal to the work surface, $\Theta = 0^\circ$.

Modulation:

Modulation is performed in an open-loop as the rotational speed is constant. Any attempt to close the loop could potentially introduce unnecessary jitters. Additionally, the inertia of a rotating, balanced M1 will further keep the speed stable and undisturbed.

Arc modulation information is compiled from slicing the layer and then rendering the layer with arcs, the radius of each arc is R , the distance between M1 and M2. Each layer data is saved in an array. Hence, a layer rendering information is contained in a two-dimensional array $Arc[i][j]$ where i is the arc number and j represents a pixel within the arc.

The modulation is performed by turning the laser beam on or off with a set time interval between the pixels (or voxel for 3D print). As the rotational speed is constant, the pixels are turned on and off in a set location dictated by time delay between pixel to pixel. This direct modulation ensures a linear mapping of the pixels to the work surface.

Temperature Prediction:

The Øgon™ deposits equal energy for any voxel across the work surface where the heat gradient is vertical at all times. The raster method further helps in having a uniform temperature distribution across the work surface.

The Øgon™ can be challenged if using a print arc that opens more than $\pm 33^\circ$ as the total pixels per area will increase slightly, therefore changing energy uniformity. In this specific example, the neighboring pixels from the two arcs will be at a distance of $0.92D$ where D is the distance between the arcs and $S(n)$ the distance between two pixels on the neighboring arcs as shown in Figure 8. Also, Figure 8 illustrates how $P1(n)$, the pixel from the present arc location, compares to $P2'(n+1)$ of the neighboring pixel from the next arc. This issue is addressed by the slicing algorithms, which adjust the energy deposition per pixel based on its location on the arc. This keeps energy uniformity all across the surface.

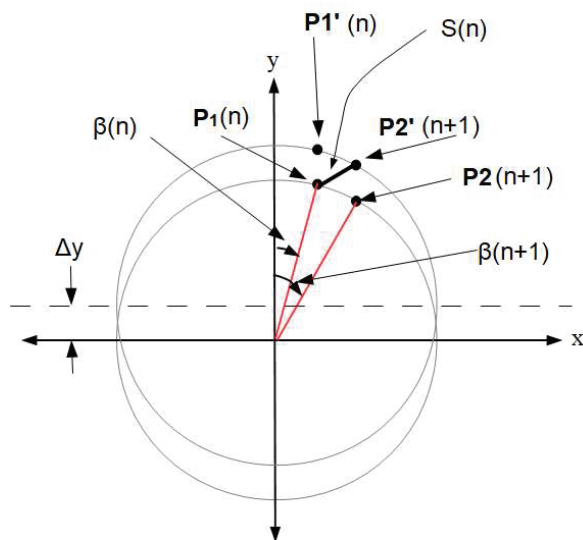


Figure 8. $P1(n)$ and $P2'(n+1)$ proximity

The distance $S(n)$ is calculated by:

$$S(n) = \sqrt{(R \cdot \sin((n+1)/P \cdot 2 \cdot \pi) - R \cdot \sin(n/P \cdot 2 \cdot \pi))^2 + (D + R \cdot \cos((n+1)/P \cdot 2 \cdot \pi) - R \cdot \cos(n/P \cdot 2 \cdot \pi))^2} \quad (15)$$

Where R , is the arc radius, D is the hatch distance, P is the number of pixels in one complete revolution, n is the present arc, and $n+1$, the next arc.

Stability:

The M1 concave surface structure shifts the center of mass from the actuator rotational axis. The M1 reflector is carried by a jacket stabilizer to keep the center of mass along the optical axis. Hence, overcoming any motor drift if it exists.

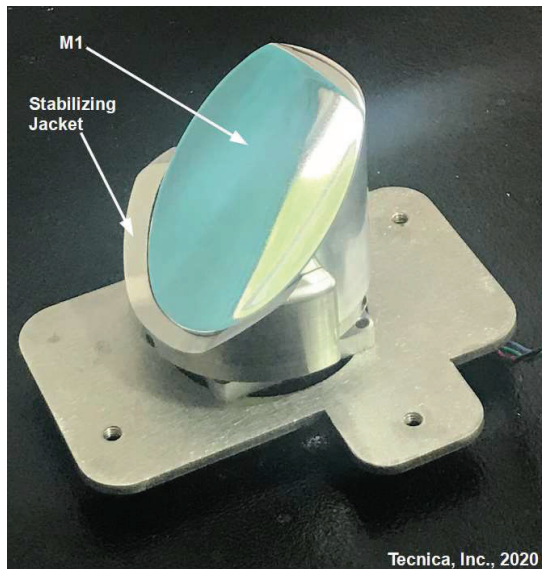


Figure. 8 - M1 with stabilizing Jacket mounted on a motor

Results and Discussion

The AM industry has attempted to mitigate Θ -related errors by several methods, each of which reduces the maximum value of Θ required for the work surface.

One method is to increase the distance d from the GS to the work surface. However, this produces bulky printers that make the design of the optics more challenging, because they have increased sensitivity to noise and magnified offset/drift errors.

Another popular method to reduce the maximum value of Θ is to use multiple lasers working in parallel. This obviously reduces print time. However, it also increases the complexity of the pre-print algorithms for two reasons. First, they must calculate multiple print paths, one for each laser. Second, the stitch lines between adjacent lasers' print areas lie at the edge of each laser's

range, where all the theta-related errors discussed above are at their maximum. Complex engineering and computational work is required to ensure that the voxels on the stitch lines are correctly aligned and receive the correct amount of energy.

Metal printing requires a high degree of temperature uniformity all across the print surface. The GS needs to address multiple causes to mitigate the heat nonuniformity. The Øgon™, on the other hand, eliminates the major causes of the problem.

Conclusions

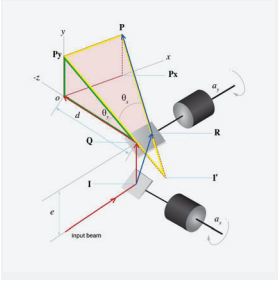
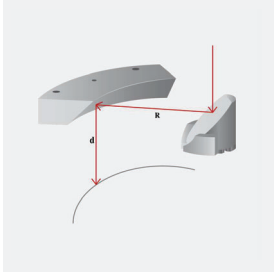
	GS	Øgon
<i>Feature</i>		
<i>Energy density</i>	★★★★☆ $\sim E_0 \cdot \text{Cos}^4(\Theta)$	★★★★★ E_0
<i>Temperature predictability</i>	★★★★☆	★★★★☆
Θ	★★★★☆ $f(\theta_x, \theta_y)$	★★★★★ Normal to the surface
	$\arccos\{1/[(\sqrt{1 + \tan^2(\theta_y)} + e/d) \cdot \sqrt{\tan^2(\theta_x) + 1 - e/(d \cdot \cos(\theta_x))}]\}$	0°
<i>Beam dimension</i>	★★★★☆ $f(\theta_x, \theta_y)$	★★★★★ Always constant r_0
<i>OPL</i>	★☆☆☆☆ $f(\theta_x, \theta_y)$	★★★★★ Always constant $2 \cdot (d + R)$
	$(d \cdot \sqrt{1 + \tan^2(\theta_y)} + e) \cdot \sqrt{1 + \tan^2(\theta_x)}$	
<i>Position</i>	★★★★☆ Nonlinear	★★★★☆ Linear & Symmetrical
<i>Speed</i>	★☆☆☆☆ Nonlinear	★★★★☆ Linear
<i>Modulation</i>	★★★★☆	★★★★☆
<i>Stability</i>	★★★★☆	★★★★☆
<i>Scalability</i>	★★★★☆	★★★★☆

Table 2: Head to head comparison between the GS and the Øgon™

The head-to-head analysis in this paper has shown that the Øgon™ Lens Free Optical Scanner solves the galvanometer scanner's fundamental problem of inconsistent energy deposition. While the surface beam speed, optical path length, and angle of incidence (which affect the beam size and shape) vary as the galvanometer scans the work surface, these properties remain constant as the Øgon™ operates.

The Øgon™ provides constant energy deposition and therefore uniform surface temperature, making it ideally suited for AM metal printing.

References

- [1] Mirkoohi E. et al, 2018, 'Thermal Modeling of Temperature Distribution in Metal Additive Manufacturing Considering Effects of Build Layers, Latent Heat, and Temperature-Sensitivity of Material Properties'
- [2] Yang D., et al, 2019, 'A model for predicting the temperature field during selective laser melting', Results in Physics Volume 12, March 2019, Pages 52-60
- [3] Jinqiang N. et al, 2019, 'Analytical modeling of 3D temperature distribution in selective laser melting of Ti-6Al-4V considering part boundary conditions', Journal of Manufacturing Processes Volume 44, August 2019, Pages 319-326
- [4] Alexander I., et al, 2014, 'Computer aided optimisation of the thermal management during laser beam melting process' Physics Procedia, Volume 56, 2014, pp. 390-399
- [5] Bibas C., 2020, 'Effects of galvanometer laser scanning system on the structural integrity of 3D printed parts.', figshare. Preprint. <https://doi.org/10.6084/m9.figshare.12318698.v1>
- [6] Huang Jigang, Qin Qin, Wang Jie, and Fang Hui, "Two Dimensional Laser Galvanometer Scanning Technology for Additive Manufacturing", International Journal of Materials, Mechanics and Manufacturing, Vol. 6, No. 5, October 2018
- [7] Xianyu Meng et al, 2019, '2-D Scanning Galvanometer Error Analysis and Its Correction', J. Phys.: Conf. Ser. 1345 022068
- [8] Zhang W. et al, 2019 Mar 18, 'An Online Calibration Method for a Galvanometric System Based on Wavelet Kernel ELM. Sensors (Basel)', 19(6):1353. doi: 10.3390/s19061353. PMID: 30889895; PMCID: PMC6471072.
- [9] Duma, V. F., 2019, 'Laser scanners with oscillatory elements: Design and optimization of 1D and 2D scanning functions.', App. Math. Model. 67 (2019) 456-476.
- [10] Bibas C., 2019, 'Beam director with improved optics', US Patent 10,416,444
- [11] Bibas C. et al., 2016, 'Beam director', US Patent 9,435,998